Laser ablation in liquid: Heating, diffusion, and condensation

Laser ablation in liquid: Heating, diffusion, and condensation

V A Khokhlov[1], N A Inogamov[1,2] and V V Zhakhovsky[2,1]

[1] Landau Institute for Theoretical Physics of the Russian Academy of Sciences, Akademika Semenova 1a, Chernogolovka, Moscow Region 142432, Russia
[2] Dukhov Automatics Research Institute (VNIIA), Federal State Unitary Enterprise, Sushchevskaya 22, Moscow 127055, Russia

E-mail: v_a_kh@mail.ru

Abstract. Laser ablation in liquid (LAL) is important technique, which is used for formation of nanoparticles (NP). The LAL processes cover logarithmically wide range of spatiotemporal scales and are not fully understood. The NP produced by LAL are rather expensive, thus optimization of involved processes is valuable. As the first step to such optimizations more deep understanding is necessary. We employ physical models and computer simulations by thermodynamic, hydrodynamic, and molecular dynamics codes in this direction. Absorbing light metal expanding into transparent solid or liquid dielectrics is considered. We analyze interplay between diffusion, hydrodynamic instability, and decrease of surface tension down to zero value caused by strong heating and compression transferring matter into state of overcritical fluids. The primary NPs appear through condensation during expansion and cooling of diffusion zone or pure gold vapor zone when pressure in these zones drops below critical pressure for a metal.

1. Introduction

Paper presents theoretical and simulation results on laser ablation in liquid (LAL) or into initially solid transparent dielectrics; gold–water and gold–silica pairs are investigated. We consider and compare ultrashort $\tau_L = 100$ fs and subnanosecond $\tau_L = 50$ ps pulses $I(t) = I_0 \exp(-t^2/\tau_L^2)$ and vary absorbed fluence $F_{\rm abs} = \int_{-\infty}^{\infty} I_{\rm abs}(t)\,{\rm d}t$ in a wide range up to values limited by optical breakdown of dielectrics; threshold values for breakdown are $I_{\rm inc} \sim 10^{11}$ W/cm^2 for the subnanosecond case with $h\nu \approx 1.2$ eV [1, 2]. LAL is used to prepare colloidal solutions of nanoparticles (NP). These processes have many technological applications, see detailed reviews [3, 4].

In spite of numerous applications and many peoples involved in working in this direction, a lot of problems remain poorly understood. This is because the ultrafast early stages still are unobservable experimentally. Only rather late stages starting from the microsecond (μs) time scale are carefully documented [5] and are described theoretically using Rayleigh–Plesset equation. Our approach developed below covers stages before the first microsecond. The late stages relates to formation and development of a cavitation bubble. The pulse durations from 0.1 ps to a few ns are from 7 to 3 orders of magnitude shorter than the experimentally observed temporal range.

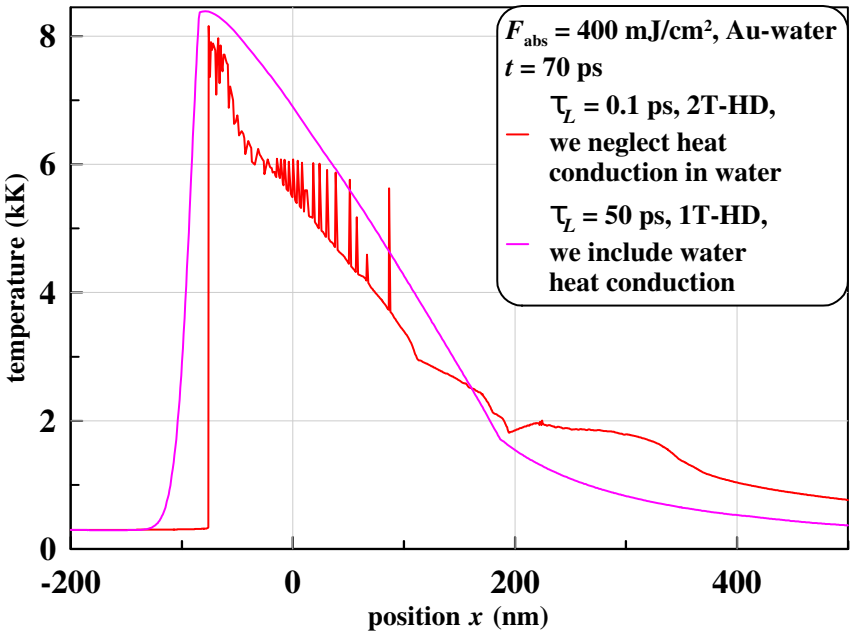

Figure 1. The temperature distribution in two cases, which differ greatly in the duration of the laser pulse. For the ultrashort pulse, the two-temperature (2T) hydrodynamics (HD) code is used [10, 11] and the profile of the ion temperature $T_i(x)$ at $t = 70$ ps is shown. In case of subnanosecond pulse $\tau_L = 50$ ps the 2T effects are of minor significance. And so, the one-temperature (1T) HD code is employed; the profile $T(x)$ at $t = 70$ ps is presented; in the 1T approximation we have $T = T_i = T_e$. Thermal conductivity of water is included in the 1T-HD code. Temperature and heat flux are continuous at the contact boundary (CB) between gold (Au) and water. Thermal diffusivity $\chi_{\rm wt}$ of water is more than 2 orders of magnitude less than $\chi_{\rm Au}$ of molten Au. Therefore, only a thin layer of water near CB heats up to the moment shown.

Recently, computer simulations shed light on the beginning of the "hidden era", continuing from the initial stage up to the time range $t < 1$ μs before the bubble begins to form [6–11]. Ultrashort pulses with duration $\tau_L = 0.1$ ps and picosecond pulses $\tau_L = 10$ ps [9] were considered, and the processes have been followed up to few nanoseconds in [6–9] and up to 200 ns in [10,11]. In all these papers the absorbed energies $F_{\rm abs}$ were comparable and of the order of ~ 0.5 J/cm^2. In the present paper we analyze new case with the three order of magnitudes longer pulse relative to durations 0.1 ps and five times longer than duration 10 ps considered in [9]. Let us mention previous papers [12–15] devoted to consideration of laser heating of metal through solid transparent media.

At first glance, it seems surprising that dynamics at the stage beginning after instant $t = 50$ ps (when the 50 ps pulse is ended) is similar in the cases with so different durations τ_L (0.1 ps versus 50 ps) if energies $F_{\rm abs}$ are the same (in more details this question is discussed below). This is what we find comparing the cases with $\tau_L = 0.1$ ps and $\tau_L = 50$ ps, figure 1. Thermal diffusivity $\chi_{\rm Au}$ of gold is large at the two-temperature (2T, $T_e > T_i$) stage [11] relative to its one-temperature (1T, $T = T_e = T_i$) values in solid and liquid states. But duration of the ultrashort pulse and duration of a 2T stage are shorter than duration 50 ps of the subnanosecond pulse. Therefore thicknesses of the heat affected zones are approximately the same in both cases shown in figure 1.

Thicknesses of the liquid layers are approximately the same in figure 1. The thin layer separating liquid and solid gold (this is the melting front) has position $x \approx 200$ nm in both cases

at the instant shown. Our model of heat conduction includes the change of thermal conductivity caused by melting. Therefore the gradient ∇T is smaller in the solid. For the same reason the gradient ∇T has a sharp kink at the gold–water (Au–wt) contact boundary (CB), figure 1. Saying here "for the same reason" we mean that the jump in temperature gradient ∇T at the contact is caused by difference in thermal conductivities of water relative to hot liquid gold.

As was said, the thermal distributions are similar in the cases with the durations $\tau_L = 0.1$ and 50 ps shown in figure 1. But there are differences also. Before saying about them let us describe a global structure of the 1D flow. In the both cases the foam region and atmosphere are formed [6–11]. The atmosphere is a layer contacting with water and being in quasi-hydrostatic equilibrium with CB as it is described in [10, 11]. The atmosphere separates foam and water. In the case of a rather long subnanosecond pulse the atmosphere forms when CB begins to decelerate. As it will be seen below, the CB accelerates during the rise of the pulse $I \propto \exp(-t^2/\tau_L^2), \tau_L = 50$ ps and some time after; we begin our simulations at the negative time instant equal to $-3\tau_L$.

In the ultrashort case shown in figure 1 the nucleation process and formation of foam begins earlier than in the subnanosecond case. This is the difference between the cases in figure 1. In the ultrashort case nucleation begins at the stage $t \approx 20$ ps while in the subnanosecond case the starting stage of nucleation is $t \approx 80$ ps. Let us mention that time is reckoned from the instant $t = 0$ corresponding to maximum of a Gaussian pulse. Nucleation and foaming for the ultrashort case (duration 0.1 ps, absorbed energy 400 mJ/cm^2) were described in [10, 11], while for the case of subnanosecond pulse with the same absorbed energy the nucleation and foaming processes are presented here below. The forest of needles seen at the temperature profile $T(x)$ at $t = 70$ ps for the ultrashort case is caused by "1D foaming". This is the representation of foaming in the 1D hydrodynamic simulations where jumps in density and temperature appears in the region occupied by foam [11, figures 15 and 16].

Nevertheless the amount of the ejected gold mass $m_{\rm ej} \approx (1.5\text{–}3)\,10^{-4}$ g/cm^2 is approximately the same in the both cases. The ejected mass forms a layer separated by a gap from the rest of a bulk gold target up to the stages $\sim 10^2$ ns. The layer contacts with water. Velocity of the layer drops down to very small values $\sim$ 1–10 m/s at the stage $\sim 10^2$ ns [10, 11]. Fate of the layer is unknown at the late stages $\geqslant \mu$s. The gap is filled by saturation vapor of gold and has pressures $\sim 10^2$–10^3 bars until gold has temperatures above ≈ 5 kK [10, 11]. While pressure in liquid and later in gaseous water is $\sim 10^2$–10^3 bars at the stage of few microseconds. Thus the gold layer may moves back under water pressure and closes the gap if the layer is cooled down below few kK. The layer may stick back with the bulk gold if gold in the layer remains liquid during the shrinkage of the gap. Velocity change Δv of the layer under pressure difference Δp acting onto the layer from its internal (vapor of Au in the gap) and external (CB, water) boundaries is large $\Delta v = \Delta p\, t_{\mu s}/m_{\rm ej} \sim 3$ km/s for $\Delta p = 10^2$ bars, $m_{\rm ej} = 3 \times 10^{-4}$ g/cm^2, and $t_{\mu s} \sim 1$ μs. Such velocities easily may close the gap during μs because the gap thickness is $\sim \mu$m only. This problem obviously needs separate consideration.

Below we will limit ourself with comparative analysis of the early ($\sim$ 10 ps) and middle ($\sim$ 1 ns) stages of the ultrashort Au–water and subnanosecond Au–water and Au–glass cases. There are two main conclusions following from this analysis.

First. All these three cases are similar in the sense of energy distribution in the surface layer, the value of ejected mass, and the trajectory of the CB $\zeta(t)|_{x=x_{\rm CB}(t)}$, where the ζ stands for kinematic (x, v, g—shift, velocity, acceleration) or for thermodynamics (ρ, p, T) quantities.

Second. The states near the CB during the middle stage about 1 ns are hot and compressed, thus both the gold and, of course, the water (with its low critical parameters) are in overcritical states relative to their critical pressures. Therefore Au–water surface tension coefficient is zero and diffusion is strong. Rather thick diffusively mixed Au–water layer forms around the CB thanks to that. Later in time the pressure drops due to expansion of the pressurized layer near

the CB. Condensation into clusters and liquid droplets begins as pressure decreases below the critical values for gold.

From the other hand, strong diffusion suppresses the development of the Rayleigh–Taylor instability (RTI), which will be considered in section 7. There is a limited in time interval when the RTI develops [10, 11] (section 3). Thus if the development is delayed during this temporal interval then contribution of RTI remains insignificant. Significant contribution from RTI into the nanoparticles (NP) production was observed for ultrashort actions and smaller (than in this paper) absorbed energies in [8–11].

In the present paper, we want to understand dynamic and thermal phenomena triggered by laser heating of a metal target irradiated across liquid. With this understanding we describe the synthesis of colloids through diffusion, cooling, and condensation processes proceeding during dynamic and thermal transformations.

The paper is organized as follows. First in section 2, we consider separation of large distances covered by shocks in gold and water from small distance passed by contact boundary (CB). This gives to readers an image of a global picture consisting from very wide shock compressed volumes in liquid and metal relative to narrow region occupied by contacting hot liquid and hot metal. Velocity of a CB decays in time quickly while shocks propagate at velocities above speed of sound. This is why huge difference in spatial scales is formed.

In section 3, the acceleration stage is considered (acceleration of the contact). It lasts during laser action. Thus this stage is different depending on pulse duration. The case of an ultrashort pulse (short, huge acceleration) differs from the case of a subnanosecond pulse (long lasting slow acceleration). Later in time (that is after the acceleration stage) these cases behave similarly if absorbed energies are the same.

In section 4, duration of the stage when parameters of a metal at the CB are in overcritical states (overcritical stage) is analyzed. It is found that this duration is a function of absorbed energy, i.e., the overcritical states exist longer if absorbed energy is greater.

We use two-temperature (2T) and one-temperature (1T) hydrodynamics (HD) codes to obtain results listed in sections 2–4. These codes were developed earlier and therefore we omit here their descriptions. The description is given in the paper [11] and in the references cited in [11]. The description includes a system of dynamical equations together with initial and boundary conditions. The codes use a Lagrangian mesh, solves dynamical, thermal, heat conduction equations and conditions and includes variable laser energy supply [11] acting in a skin-layer of absorbing metal.

Thermodynamic equation of states for gold and water are taken from the reference sources and calculation approaches presented in [16–26]. They describe matter in a wide range of thermodynamic parameters from condensed solid and liquid states to critical point and above the critical point and to gaseous states corresponding to large expansions of initially condensed matter. They cover temperatures from small values below room temperature up to high ones (10^5 K).

First order phase transitions are accurately taken into account. Latent heats of melting and sublimation and their dependence on temperature are included. Dependence of melting or sublimation temperatures on pressure (or, equivalently, on density) reproduces all known experimental and simulated data: quantum-mechanical packages are used to describe areas of phase diagram where experimental information is scarce. Dependence of saturation pressure of gold on temperature corresponds to measured data, see [11]. Coexistence curve relates experimental values of thermal expansion.

Embedded atom model (EAM) potentials of interatomic interactions and molecular dynamics (MD) simulations (EAM-MD simulations) are applied to reveal another part of valuable information in sections 5, 6 and 7. Saturation pressure, curves of equilibrium between phase states, surface tension coefficient, and description of diffusion on the base of the EAM-MD

approach are presented in section 5. Saturated vapor pressure, equilibrium curves (boiling and condensation), and surface tension coefficient obtained from the developed EAM potential for gold are compared with available experimental data and with data corresponding to the equation of state used in hydrodynamic simulations.

It is shown that EAM potential for gold used in our MD calculations gives accurate description of all listed quantities. Necessary references to the sources where the EAM for gold was presented in published and available forms are given below in the text of section 5. For correct description of condensation process it is important that the EAM potential for gold accurately presents surface tension and binding energy of two gold atoms forming a dimer Au_2.

Our model used to present water intermolecular interaction and interaction between water and gold atoms is given in section 5. Water in the model is described as a monatomic system. The EAM potential for water can be found in [27]. The EAM potential for water provides the correct mechanical properties of liquid water including the density, sound speed, and shock adiabatic curve up to few tens of GPa. This range pressures is enough for our applications.

Condensation of gold and formation of nanoparticles is described in section 6. We use EAM potentials for gold and water from section 5 and run long MD simulations to follow kinetics of decay of supersaturated gold vapor into two-phase vapor–liquid mixture. The cases of pure gold and water–gold mixture are compared. In previous analysis [28–31] authors consider condensation of vapor evaporated into vacuum or into buffer gas. These cases correspond to much lower densities and lower temperatures. In the considered here cases (corresponding to LAL—laser ablation in liquid) the condensation takes place in dense environment (due to confinement by liquid), our temperatures are more close to critical temperatures and densities are much higher. Saturation pressure exponentially depends on temperature therefore the considered cases are qualitatively different from condensation in rarefied gas.

Section 7 demonstrates results of large scale MD simulation of the ablation of gold in water. Especially the near contact events are carefully analyzed. The EAM potentials for gold and water presented in section 5 are used. It is shown that dynamic phenomena (acceleration and deceleration of contact, water resistance to expansion of gold), thermal phenomena (laser heating, heat expansion, phase transitions), diffusion between gold and water—all together form a set of interaction processes which accompany and finally define the rate of appearance and size distribution of produced nanoparticles. Thus condensation into nanoparticles is considered as a result of a chain of real complicated transition events.

2. Global and internal structures

Global structure of flow is clear from figure 2. Before action of a pulse we have two motionless half-spaces in contact. The left one $x_0 < 0$ is filled with water, while the right one $x_0 > 0$ corresponds to the bulk gold target; here x_0 is Lagrangian coordinate; it corresponds to initial (before laser action) positions of material particles. Laser beam penetrates through transparent water and heats absorbing gold in its skin-layer. Heating causes the pressure rise while the gradients of pressure in their turn cause motion. After finishing of a pulse the spatial expansion gradually decreases pressure. Two shock waves (SW) in figure 2 run into water and into gold target. The pulse is rather long $\tau_L = 50$ ps. Therefore it takes some time to form the shocks. The SWs form thanks to nonlinear effects after focusing of characteristics and wave breaking. Velocity "jump" 0.23 km/s in figure 2 covers the layer where the atmosphere and foam locate. This "jump" characterizes expansion of the contact boundary relative to the bottom of the foam at the instant of 0.5 ns. This velocity is small (just few %) in comparison with velocity $c_s|_{\mathrm{Au}} + c_s|_{\mathrm{wt}} = 4.5$ km/s giving the lowest limit of velocity of the increase of the distance between two shock waves in figure 2. Expansion of foam proceeds as a result of easy extensibility of a vapor component in foam. Structure of the thin layer near the CB (the "jump" in figure 2) is revealed in figure 3.

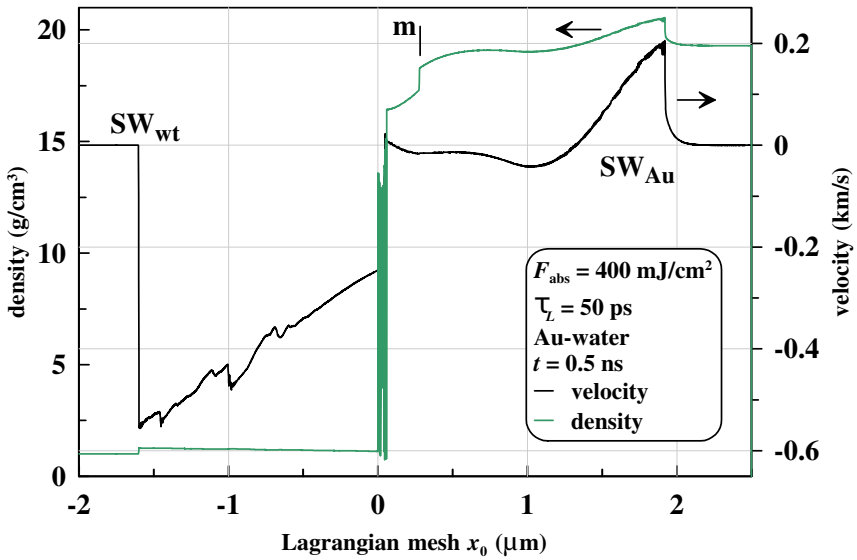

Figure 2. Density and velocity profiles are shown. Point "m" indicates current position of the boundary between solid and liquid gold. We see that at the stage after ~ 1 ns the near contact layer is much more thinner than the region between the two SWs (SW_{Au} in gold and SW_{wt} in water). The profiles are plotted as functions of initial positions x_0 of material particles of gold and water. Thus reader can easily estimates masses. E.g., current mass of shock compressed water is $x_0|_{SW-wt}\,\rho_0|_{wt}$, where $x_0|_{SW-wt}(t)$ is position of the SW in water, $\rho_0|_{wt}$ is initial density of water. Lagrangian positions are motionless; $x_0 = 0$ is the contact boundary (CB).

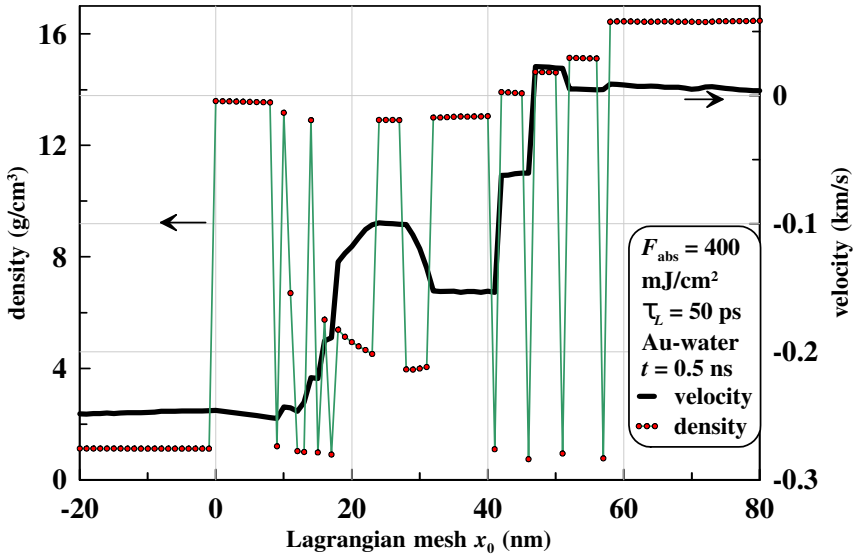

Figure 3. Internal structure of the foamy layer near the CB, which is shown in figure 2. We see how the velocity "jump" from figure 2 is accumulated along the stretching foamy layer. Inertia of gold supports this stretching at the temporal stage shown. Small red circles mark positions of the steps of the Lagrangian mesh. The mesh should cover large distances passed by SWs. Nevertheless it satisfactory describes foaming—there are few mesh points per every liquid peace of the foam.

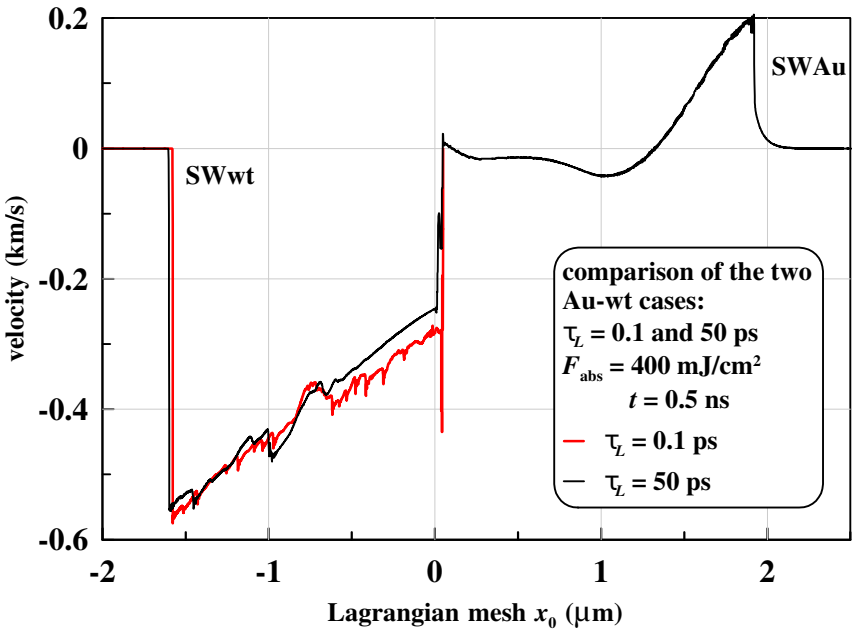

Figure 4. Comparison of the velocity profiles for two very different durations of laser action. The velocity profile for the simulation with $\tau_L = 50$ ps is taken from figure 2.

Comparison of our Au–water simulations for ultrashort laser pulse $\tau_L = 100$ fs [10, 11] and subnanosecond pulse with $\tau_L = 50$ ps is demonstrated in figure 4. Absorbed energies are the same. We cut out the slowly moving part of bulk gold in the ultrashort case [10,11]. Only really significant for mixing with water and nanoparticles production part of a gold target was kept in the simulation of ultrashort action. Comparing two simulations in figure 4 we conclude that:

First, at the nanosecond time scale and later the duration of a laser pulse varied 500 times from 0.1 to 50 ps is insignificant.

Second, the passive part of the gold target kept in one simulation (pay attention to the SW running into bulk in figure 4) and removed in the another one is, indeed, insignificant for dynamics of foam and water.

But internal structures of density distributions inside the foamy layer differ, figure 5; we compare the cases with different pulse durations 0.1 and 50 ps. This is not surprising. Indeed, durations differ 500 times. Nucleation starts at different instants: 20 and 80 ps, respectively, and proceeds through different ways because the conditions outside to the foamy layer are different. Let us mention that hydrodynamic simulation accurately describes nucleation and foaming. This was proved by comparison with experiments and molecular dynamics (MD) simulations [11,32]. If the computational cell used in MD is narrow in transverse (to main motion) directions then the foamy region in MD also (as in hydrodynamics) looks like the chain of the condensed and gaseous pieces, see, e.g., [33]. To describe nucleation and foaming in hydrodynamics we use concept of finite material strength. The material strength is a value of tensile stress $p_{\rm lim}$ above which material begin to decompose. The strength $p_{\rm lim}$ is temperature and deformation rate dependent. We run special MD simulations [34] for gold under tensile stresses at different temperatures for deformation rates typical in our conditions of laser actions. Thus the strength was defined. In our calculations presented here we use expression (12) from [34] for the strength.

Expansions in water (liquid dielectrics) and in glass (initially solid dielectrics) qualitatively are similar up to the stage when in the case of water the bubble begins to form. Corresponding situations are shown in figure 6. Transparent for laser light dielectric materials—solid or liquid—

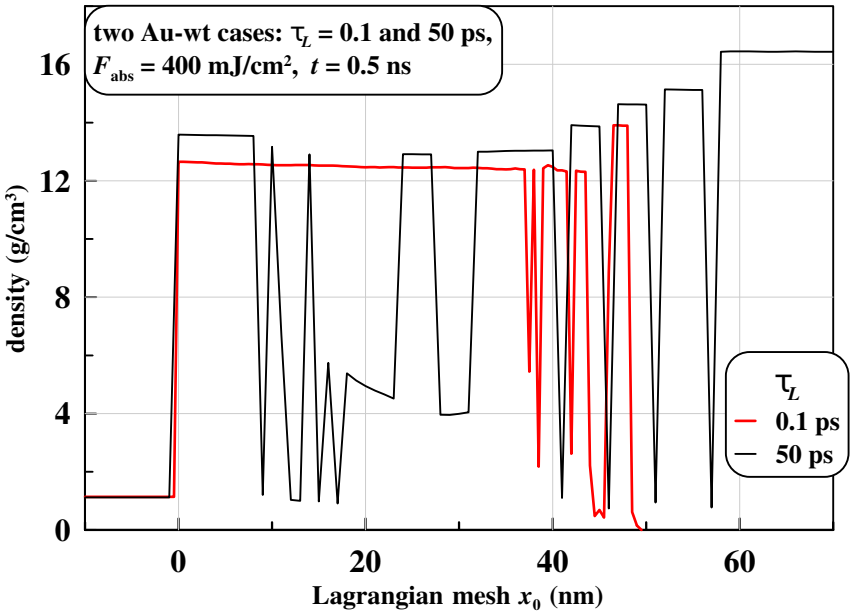

Figure 5. Density structure in foamy region for the two cases compared in figure 4.

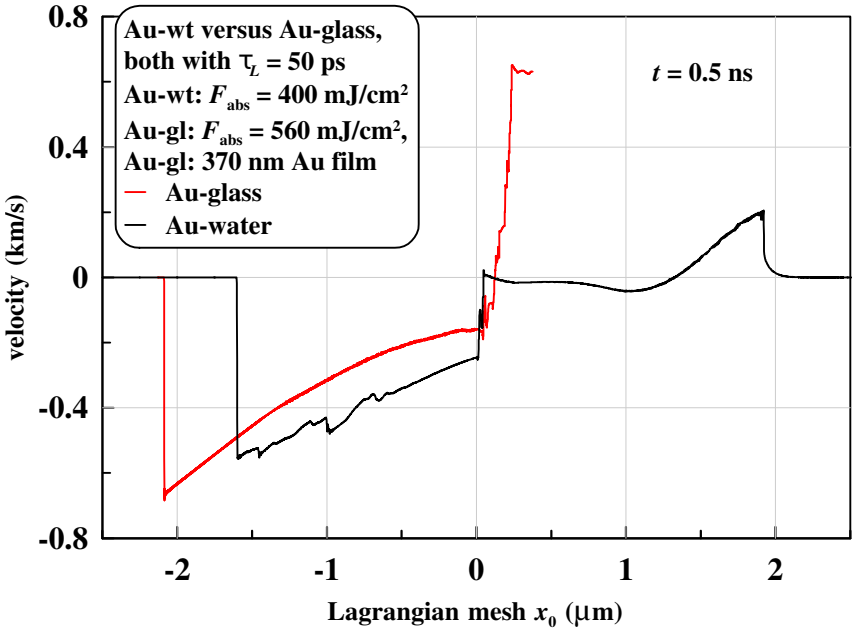

Figure 6. Velocity profiles for the instant 0.5 ns for the Au–water and Au–glass cases of the same duration 50 ps.

are similar in their dynamic behavior under action of laser onto an absorbing target covered by the dielectrics. Their behaviors are similar at the initial and middle stages, when compression stress is higher than an elastic limit for solid dielectrics. Then solid behaves plastically in unidirectional compression as does liquid. Therefore at these stages the dynamic behaviors are similar. Typically the elastic limit for solids is of the order of fraction or one GPa, i.e., ten thousands of bar. At the late stage in the case of liquid dielectrics a process of bubble formation starts. This process begins when the compression stress decreases in our case with water down

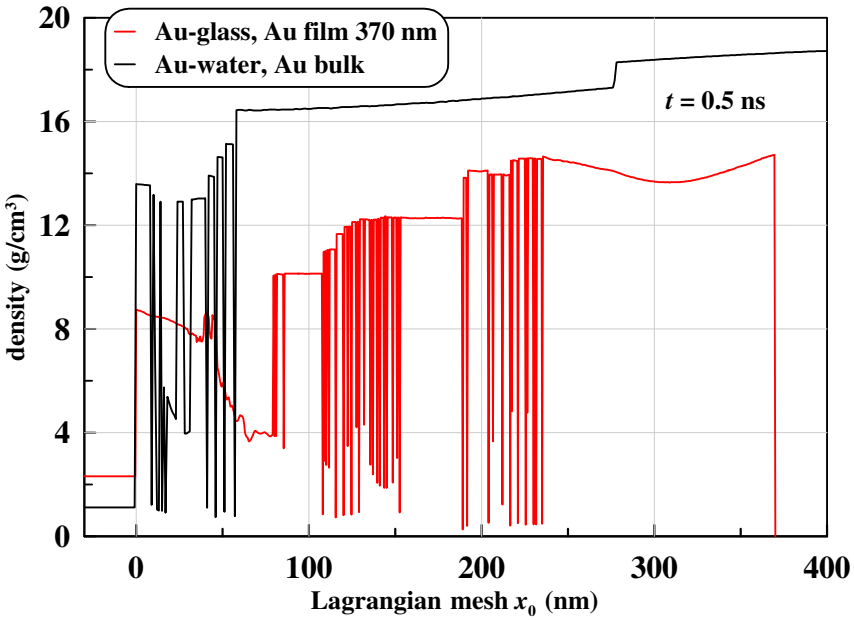

Figure 7. Density profiles near the CB for the same two cases as in figure 6.

to values of the order of critical pressure for water 220 bar, i.e., 0.022 GPa. Of course, at this late stage solid dielectrics behave very differently relative to the liquid ones. Therefore, obviously, the similarity between their behaviors is ceased.

In figures 6 and 7 the cases with a bulk gold target and a thick film target (initially 370 nm thick) are compared. We call a film thick if its thickness is larger than thickness of a heat affected zone (HAZ) [35, 36]. Thickness 370 nm is larger than thickness of HAZ, figure 1. The case with a film 370 nm and a glass substrate is considered in connection with experiments [37, 38]. Discussion in connection with these experiments needs separate description. Figures 6 and 7 demonstrate dramatic difference between the cases with a bulk and a film targets if we consider motion of gold; dynamics of dielectrics are similar as it follows from figure 6. Initially the system from dielectrics and a target was motionless, thus its momentum is zero. Laser beam introduces energy $F_{\rm abs}$ into the system, but not momentum because momentum of a photon cloud is negligibly small. Therefore total momentum of a system is zero after laser impact.

The momentum directed into the side of dielectrics produces motions in dielectrics which are more or less similar in both cases, see figure 6. But the motions in the gold targets triggered by the right side momentum are very different depending on thickness of a film. In a bulk target this momentum is carried into the bulk side and out from the near CB layer by approximately triangular shock wave $\rm SW_{Au}$ in figures 2, 4, and 6. In the case of a film this carryover is impossible—thickness is limited. Thus all amount of the powerful push to the right remains in a film. This causes decay of a film into a sequence of quasi-spalled plates separated by foamy layers in case of a film, see figure 7. Velocity of the rear-side plate is large, see figure 6.

We follow carefully every successive in time frames of our HD simulations of a thick film above a glass substrate; thus we know how the flow evolves; only few frames are shown as illustrative figures in the paper. We use nucleation criterion based on material strength of gold described in paper [34]. We see how the tensile stress gradually increases, how it achieves the limiting strength, and how the Lagrangian chain of numerical cells in the Lagrangian 1D mesh is cut by our algorithm in two separate parts: to the left part and to the right part relative to the point where the chain was broken. At the edges of these parts the dynamical boundary condition with small or zero pressure is imposed after breaking. The low density gap between these edges

appears. But for strong rarefaction wave the process does not ceased after formation of the first gap. Again at some distance from the low pressure boundary condition the tensile stress appears and begins to increase in its amplitude. It again achieves the critical value and a new spallation layer is formed. Thus formation of a few spallation layers is possible and for strong and rather long (subnanosecond) action this indeed takes place, see [39, 40] where this phenomenon was also observed. The gaps are filled by foam.

Some evidence of existence of condensed relatively cold spallation plates intermitting with foamy layers follows from experiments done in Marseille university, see papers [37,38]. They saw cupola like frozen structure together with narrow angle spread, slow moving jet consisting from pieces. The last spallation plate in our simulations moves slowly thus it have time to be frozen at the surface. The faster liquid condensed plates transform into the pieces of rather slow moving jets. The pieces are intermitted—this is the traces of foamy layers. The jet cannot be trace of hot plasma like layer. The plasma like layer will expand wider relative to angle distribution and faster. In [37, 38] authors see transition to the plasma like jet at very high absorbed energies when a hole in a film (not the frozen cupola) remains.

In our sequence of simulation frames we see definitely that the gaps between the condensed pieces (the sequence of the spalled plates) expands geometrically while the condensed pieces remains intact—gradient of expansion velocity is zero inside the condensed pieces (if we average this gradient over time—because the pieces oscillates—sound waves propagate inside the pieces, oscillation period is $\sim d/c$, where d is thickness of the condensed plate, c is the speed of sound). Therefore average density of foam gradually drops down. At the rather late stage (0.5 ns) this average density decreases to low values thanks to expansion.

3. Active dynamics: Acceleration, deceleration, and comparisons

The dynamics of CB expansion in the case of Au–water pair is shown in figure 8, where cases with ultrashort and subnanosecond laser pulses are compared. Absorbed fluences are the same 400 mJ/cm^2. In both cases intensity is given by the Gaussian law $I \propto \exp(-t^2/\tau_L^2)$. But durations τ_L differ 500 times. Thus if we impose these Gaussian laws onto the plane in figure 8 then the subnanosecond pulse will have visible left and right wings. And the rise of its left wing is proportional to the growing shift of CB in the subnanosecond case. While the Gaussian for the ultrashort pulse looks like delta-function at the temporal scale used in figure 8.

The speed up interval is very short for the pulse with $\tau_L = 0.1$ ps. We do not see it because the time scale in figure 8 is too large. At this scale, it seems that in the ultrashort case the CB starts to move immediately at the instant $t = 0$ with large velocity. Later in time $t > 0$ it only decelerates thanks to resistance of water to expansion of gold. But in the subnanosecond case the definite acceleration stage exists. Of course, it is related to the increase in time of absorbed intensity at the left wing of Gaussian pump.

Effect of absorbed energy, resistive ability of dielectrics (i.e., its ability to resists to expansion of gold), and thickness of a gold target on the trajectory of the contact boundary $x_{\mathrm{CB}}(t)$ is illustrated in figure 9; resistance of dielectrics causing deceleration of expanding gold is higher if the decelerating material is more dense. Obviously, the shift increases if we increase absorbed energy fixing two other parameters: density of dielectrics and thickness of a gold layer. If we increase density of surrounding medium then deceleration is faster; initial density of the pyrex silica used in our Au–glass simulations is 2.2 g/cm^3. Compare the cases water, 400 mJ/cm^2 and glass, 560 mJ/cm^2 in figure 9. This is also obvious.

Less obvious are consequences of variation of thickness of a layer of Au. It seems, at first sight, that a thick target will decelerate more slower. But there is foam formation and appearance of a contact layer of gold (atmosphere) [10, 11]. Speed of sound in foam is low. The first portions (atmosphere) of fragmented Au are decelerated by surrounding water or glass, while the second portions move faster thus adding their mass to the first portions located at the CB. This is said

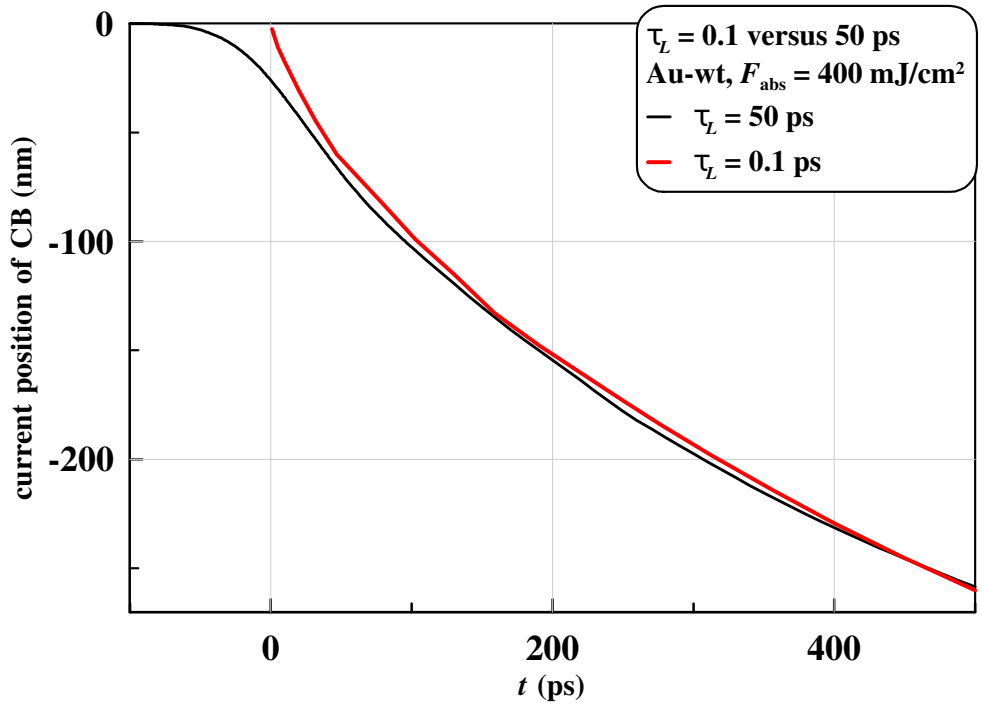

Figure 8. In this picture we compare the ultrashort and subnanosecond actions onto the Au–water system. Thus this picture is similar to figure 4. We use the same colors for these two cases as in figure 4. Let us emphasize remarkable similarity of these cases as it was already mentioned in figure 4. The trajectories are very similar if we exclude the speed up interval $t < 0, |t| \sim \tau_L = 50$ ps for subnanosecond drive.

to underline that there is a decelerated layer (atmosphere) and its mass $m_{\rm ej}$ may change with time.

Analysis of simulations show that asymptotically velocity v and pressure p at the CB are acoustically connected $p = Zv$, where $Z = \rho c_s$ is acoustic impedance in surrounding medium. Writing $m_{\rm ej}\ddot{x} = -Z\dot{x}$ we find that $\dot{x} \propto \exp(-t/t_{\rm dec})$,

$$t_{\rm dec} = m_{\rm ej}/Z \approx (\rho_{\rm Au}/\rho)h_{\rm ej}/c_s, \tag{1}$$

where x is CB position, ρ and c_s are the density and the speed of sound of surrounding matter. The estimate (1) gives for the deceleration time constant a value $t_{\rm dec} = 0.7$ ns for density ratio $\rho_{\rm Au}/\rho \approx 10$, height of atmosphere $h_{\rm ej} \approx 100$ nm, and speed of sound in water $c_s = 1.5$ km/s.

Another important conclusion from figures 8, 9, and the estimate (1) for the deceleration time constant $t_{\rm dec}$ is that in all cases the shift $x_{\rm CB}$ is very limited—it is just of the order of micron.

The difference between ultrashort and subnanosecond laser drives is distinctly visible from figure 10. Whereas there is a relatively prolonged acceleration interval in the subnanosecond case, in the ultrashort case the velocity trajectory starts from high value and after that only decelerates with time. Let us mention that in the subnanosecond case an acceleration continues after the instant $t = 0$ when the maximum of a laser pump is achieved. Thus intensity begins to decrease while velocity still increases. Increase of velocity continues approximately up to $t_{\rm max-vel} = 20$–25 ps after maximum of a pump at the instant $t = 0$.

Velocity drop in the ultrashort case shown in figure 10 is well described by a relationship $v = v_1 \exp(-0.63(t - t_1)^{0.23})$, where $v_1 = 4.05$ km/s, $t_1 = 1.1$ ps. The subnanosecond velocity

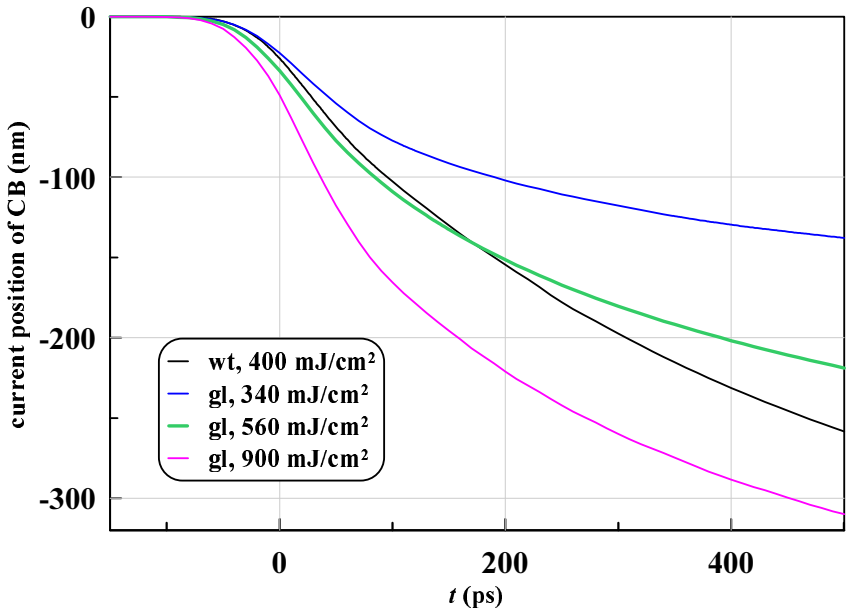

Figure 9. Trajectories of CB in four cases with a subnanosecond drive. Abbreviations "wt" and "gl" relate to the Au–water and Au–glass systems. Digits in mJ/cm^2 give absorbed energies. There is a gold film 370 nm thick in the Au–glass systems. We use a bulk gold target in the Au–water case.

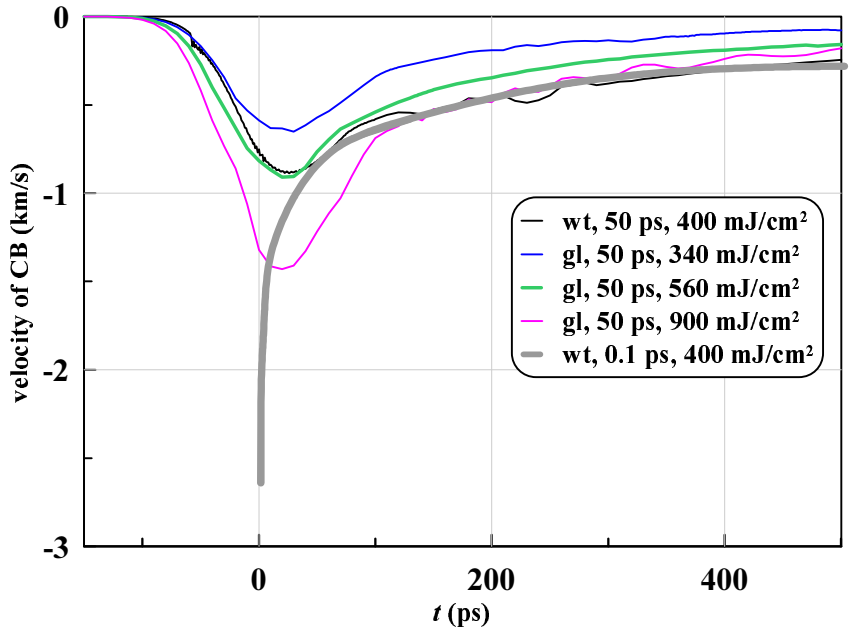

Figure 10. Velocities of contact boundary (CB) $v_{\mathrm{CB}}(t)$. Designations are similar to figure 9. The digits in ps are the e-folding durations of pulses. The picture emphasizes qualitative distinctions between ultrashort and subnanosecond pulses at the early stage. The delay of beginning of deceleration significantly influences development of Rayleigh–Taylor instability in direction of suppression.

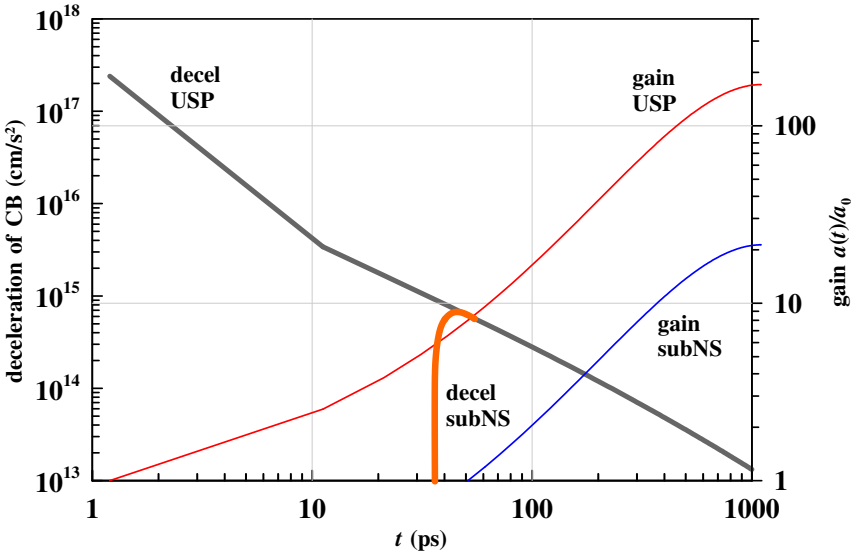

Figure 11. Deceleration of CB for the ultrashort pulse (USP) is marked as "decel USP" and as "decel subNS" for the subnanosecond pulses. In the subnanosecond case the acceleration is changed to the deceleration at the instant $t_{\max-\mathrm{vel}}$, see figure 10. After the time interval ~ 10 ps long after the instant $t_{\max-\mathrm{vel}}$ the dependence $v_{\mathrm{CB}}(t)$ asymptotically tends to the dependence for the ultrashort pulse. Thus the deceleration for the subnanosecond pulse asymptotically approximately tends to the deceleration in case of the USP. This is shown by the curve "decel subNS" starting from zero and going approximately to the $\ddot{x}_{\mathrm{CB}}$ for USP. This difference in deceleration trajectory causes delay in the Rayleigh–Taylor gain, compare the curves "gain USP" and "gain subNS" shown, these curves relate to the right vertical axis, see text for explanations.

trajectories obey the approximately same law but only after few tens of ps after their maximum of velocity $t_{\max-\mathrm{vel}}$. Deceleration dependence on time is plotted in figure 11. There is relatively slow acceleration in the subnanosecond case. The acceleration interval is lost for the Rayleigh–Taylor (RT) amplification of perturbations of CB. Thus development of the RT instability is significantly weaker in the subnanosecond case, compare the curves "gain USP" and "gain subNS" in figure 11. The temporal interval of a few tens of ps is important for development of the RT disturbances because during this interval the deceleration is huge, see the curve "decel USP" in figure 11. These decelerations overcome values 10^{14} cm/s^2 typical for surface of a neutron star. Atomic decelerations in interatomic interactions are of the order of 10^{18} cm/s^2. The curves "gain USP" and "gain subNS" in figure 11 corresponds to the wavelength 60 nm of a harmonic perturbation. They were calculated using linear RT theory including surface tension and viscosity according to the method described in [10, 11].

4. Strong heating, inertial geometrical confinement, and overcritical states

Gold is strongly heated at the end stage of absorption of a subnanosecond pulse, see figures 1 and 12. Simulations are done using equation of state for gold, water and glass taken from [16–26]. For water and glass the Hugoniot dependencies were used. They are obtained from shock wave experiments analyzed in [20,21]. Thus for water and glass we use polytrophic dependencies. For water they are given in [11, figures 8, 9 and expression (12)]. This is enough outside the very thin layers of hot water and glass near the contact. Dynamically these thin layers negligibly affect dynamics of deceleration of gold. Because the deceleration is defined by the bulk, shock compressed mass of water and gold. We use heat conduction description for gold from [11, 41].

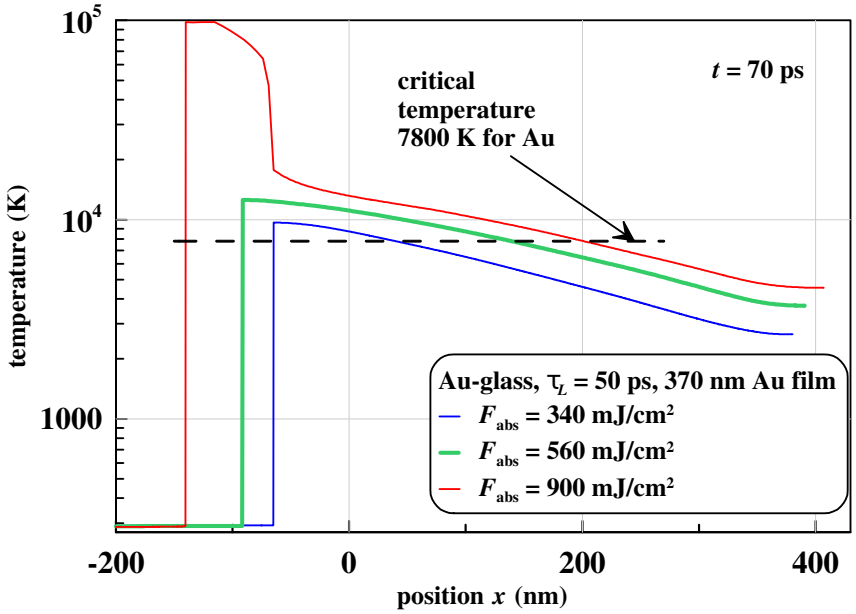

Figure 12. Maximum heating after absorption of a subnanosecond pulse. We see that for all three cases temperatures near CB are higher than critical temperature. Compare with figure 1.

The description includes calculated contribution from electron–electron collisions important at high temperatures and decrease of conductivity during melting. Critical parameters of gold are 7.8 kK, 0.53 GPa, and 5.3 g/cm^3 [16–26].

Heated gold is cooled due to heat conduction into deeper layers and thanks to adiabatic cooling during expansion. Inertial confinement by rather dense dielectric limits a rate of expansion and thus the rate of cooling. It takes approximately 0.2 ns to cool the CB below critical temperature $T_{\rm cr}$ in the case with $F_{\rm abs} = 560$ mJ/cm^2. In the case with $F_{\rm abs} = 900$ mJ/cm^2 the time interval for such cooling is longer, figures 13–15.

The temporal interval, when gold near a CB is in overcritical state, plays a special role in the process of nanoparticles (NP) formation. See discussion in the next section. Here we have to discuss strong increase of temperature near the CB (figures 12, 13) in the case of the most powerful action ($F_{\rm abs} = 900$ mJ/cm^2) from the sequence of the considered cases. It is obvious that temperature at the CB after absorption of a subnanosecond pulse $T_{\rm CB}(t \approx \tau_L)$ increases as energy $F_{\rm abs}$ increases while density $\rho_{\rm CB}$ drops down. How high is temperature $T_{\rm CB}(t \approx \tau_L)$ at the CB? From energy balance we have an estimate $T_{\rm CB}(t \approx \tau_L) \sim F_{\rm abs}/d/c$, where $d \sim 2\sqrt{\chi_{\rm Au}\tau_L}$, c is heat capacity of gold per unit of volume. Our model of heat conduction [11, 41] describes dependence of thermal diffusivity $\chi_{\rm CB}$ on density. Values of $\chi_{\rm CB}$ and c decreases as density decreases. Thus temperature $T_{\rm CB}(t \approx \tau_L)$ is not simply proportional to $F_{\rm abs}$ as it is in the case with permanent values of $\chi_{\rm CB}$ and c.

Namely nonlinear dependence of a function $T_{\rm CB}(t \approx \tau_L)$ on $F_{\rm abs}$ causes appearance of the overheated contact layer in figures 12 and 13, see also figure 15. In this layer temperature increases 5–7 times above the average level. While density drops 5–7 times below the average level, see figure 15. Thus pressure is approximately the same across the matter of glass near the CB, in the overheated layer, and in the dense gold near this layer, see figure 14.

Transport properties of gold in the states with $\rho \sim 1$ g/cm^3 and $T \sim 1$ eV are poorly known at the present state of human knowledge. Thus we cannot pretend that our conduction model [11,41] (the model gives strong decrease of thermal conductivity with decrease of density) is very accurate at these hot states of intermediate density between condensed and gaseous values. But

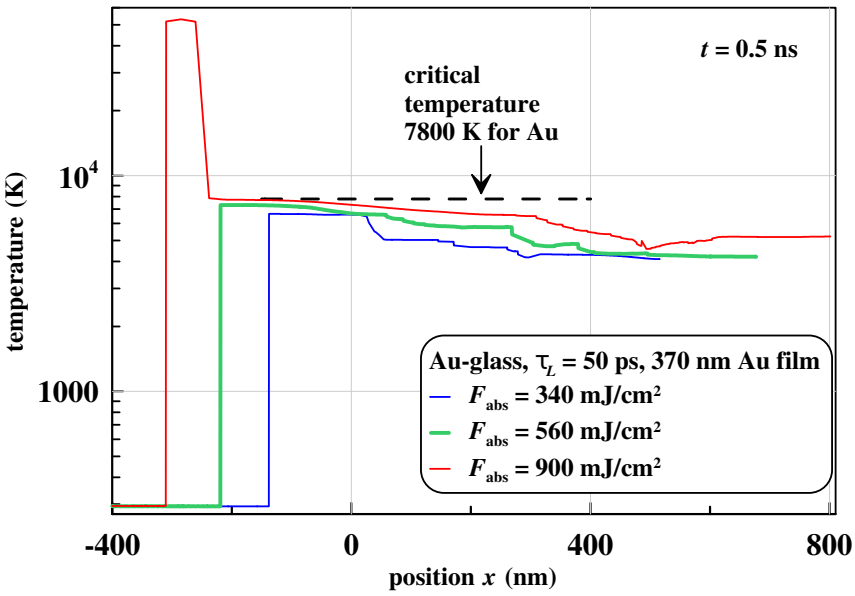

Figure 13. Gradual cooling of gold (compare with figure 12) as a result of thermal conduction and work done for mechanical expansion of matter. When the transition from the overcritical state to the two-phase states takes place and how long gold near CB exists in the overcritical state—these questions are important, because diffusive mixing is strongly enhanced in the overcritical states, thus more amount of gold is transferred into nanoparticles during cooling of a mixture since a diffusive layer is thicker. Temperature jumps at the profiles $T(x)$ at $t = 500$ ps are connected with fragmentation and formation of a sequence of liquid layers, figures 3, 5, and 7. Vapor layers in this sequence are much less conductive than liquid. Therefore temperature becomes homogeneous inside the liquid layers and jump from the value for one layer to the value of the neighbor layer.

we are sure that at least at the semi-quantitative level the model is true in these states. Therefore phenomenon with the nonlinear overheating have to take place but may be at slightly different energies $F_{\rm abs}$. If we suppose absorption of gold at the level $A = 0.3$ than incident intensity $I_{\rm inc} \sim F_{\rm abs}/A/\tau_L$ is $\sim 10^{11}$ W/cm^2, that is somewhere not far from the values corresponding to optical breakdown of dielectrics. This understanding seems limits achievable level of the highest temperatures $T_{\rm CB}$.

5. Disappearance of capillary barrier and strong enhancement of diffusion

As follows from figures 1, 12–15 the CB is above the critical point for gold for some temporal interval. Critical point of water (220 bar, 647 K, 0.3068 g/cm^3) is much lower than the critical point of gold. Thus both liquids are in the overcritical states. Then they behave like the non-ideal gases. Surface tension at the contact boundary (CB) between them becomes zero. While diffusion coefficient increases. In condensed matter the diffusion process is slow because an atom loses time doing many oscillations inside its potential well before it transhops to the neighbor well. We use molecular dynamics (MD) simulation with EAM (embedded atom method) interatomic potential (EAM-MD simulations) for gold to calculate saturation pressure (figure 16), the boiling and condensation curves (figure 17), and surface tension at the boiling curve (figure 18). We modify our previous EAM potential for Au–Au interaction described in [46]. The modified potential provides the correct dependence of surface tension coefficient on temperature shown in figure 18 and gives correct dimer Au–Au binding energy. Mechanically both potentials are close

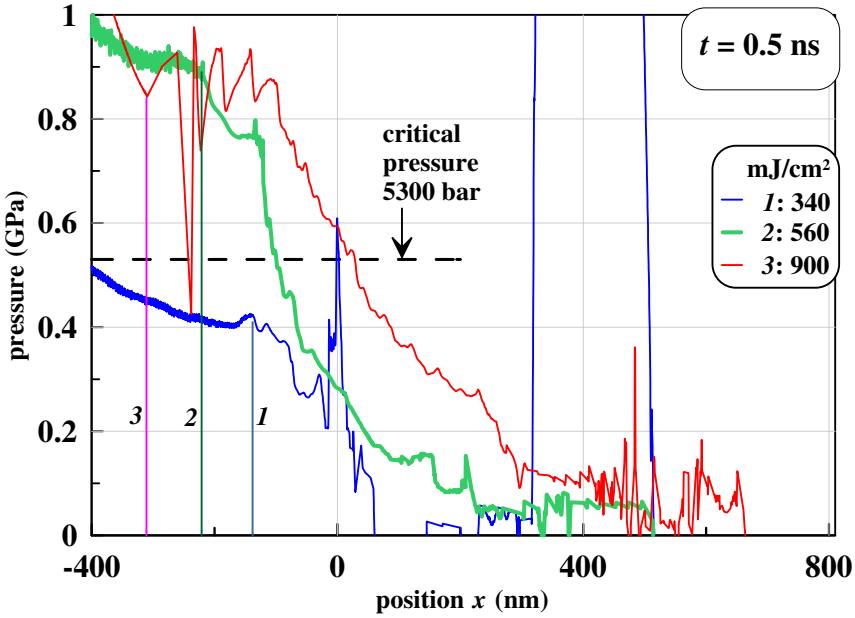

Figure 14. Pressure profiles near the CB at the nanosecond time scale. We see that only in the case with $F_{\rm abs} = 340$ mJ/cm^2 pressure drops below the critical value for Au. The vertical straight lines *1, 2,* and *3* designate current positions of the CB for the three cases considered. Simulation parameters are the same as in figures 12 and 13. The instant of time is the same as in figure 13. The CB separates dense (Au) and less dense (dielectrics) media in the cases *1* and *2*; correspondence between the digits *1, 2,* and *3* and values of $F_{\rm abs}$ is shown in the inset. Therefore in these cases the ∇p has the kink at the CB. The layers of positive and negative p (seen deeper to the right relative to the CB) of rather significant amplitudes (few GPa) are caused by oscillations of the spallation plates seen in figures 3, 5, and 7.

to each other (equilibrium density, compressibility, shock Hugoniot). Melting temperatures are very near to the experimental value for both potentials. We refer to these EAM potentials as old and new EAM potentials in figures 16 and 17 and below in the text.

Figure 16 presents the binodal curve at the T, p phase plane. We see that both EAM potentials underestimate saturation pressure at high temperatures near the critical point relative to the data from [16–26]. While critical temperature is or higher for the new EAM potential, or lower for the old one. It should be said that the exact values of critical pressure and temperature of gold still remains unknown. Thus in reality we cannot definitely conclude what set of data is more close to the real gold.

Figure 17 shows the boiling and condensation curves at the density–temperature plane, where results from equation of state (EoS) [16–26] and two EAM potentials are compared. We see that at the ρ–T plane the new and old potentials limit the EoS data from above and from below.

Molecular dynamics (MD) simulation of atom diffusion in the hot binary mixture Au–water was performed with using three different potentials describing interactions between atoms Au–Au, water–water, and Au–water. The new EAM potential was used for describing of Au–Au interactions, for which the EAM potential was developed in [11], see the data files on the project [27]. It provides the correct mechanical properties of liquid water including the density and sound speed in ambient conditions, and shock Hugoniot as well.

Due to lack of information, the interaction of Au atom and water molecule is greatly simplified to a pairwise potential between Au and "water" atoms using the van der Waals radii 0.166 nm for Au and 0.152 nm for oxygen atom, and a strong repulsion $\sim r^{-11}$ is assumed. Using a larger

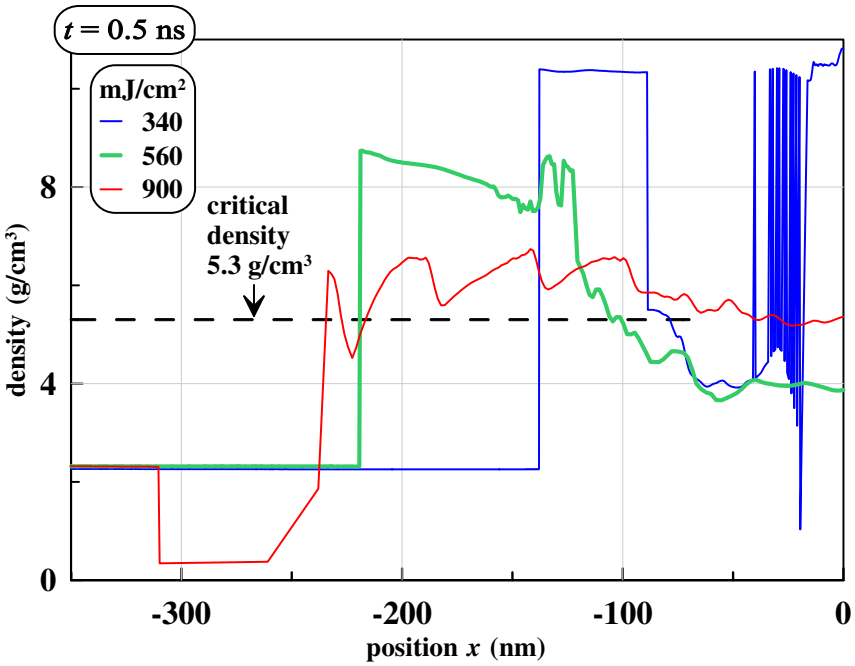

Figure 15. Structure of the near CB layers. The CB expands more in dielectric at the same instant of time as more energy $F_{\rm abs}$ is absorbed. Parameters of simulations are presented in figures 12 and 13. We see that only in the strongest case $F_{\rm abs} = 900$ mJ/cm^2 the density of gold at the CB remains below the critical density and thus at the gaseous side above the critical point at the ρ–T phase diagram. While in the two other cases these densities are at the liquid side of the diagram.

Table 1. Self-diffusion Au–Au coefficient $D_{\rm Au-Au}$ in homogeneous high-temperature state of Au at $T = 10$ kK in the overcritical states shown in figure 17 by the magenta rhombus. The last line gives the diffusion coefficient $D_{\rm Au-wt}$ of Au atom in the homogeneous Au–water mixture $T = 10$ kK with atomic partial concentrations 50 : 50 and partial densities 4.1 and 0.4 g/cm^3 of Au and water, respectively. We use new EAM in calculations.

ρ of Au [g/cm^3]	4.1	8.2	16.4
$D_{\rm Au-Au}$ [10^{-3} cm^2/s]	1.47	1	0.41
$D_{\rm Au-wt}$ [10^{-3} cm^2/s]	1.13		

van der Waals radius of 0.19 nm of water for our “water” atom reduces the diffusion coefficient of Au atoms in the simulated 50 : 50 binary mixture by about 10–20%; 50 : 50 is the ratio of the numbers of atoms per unit of volume; partial densities are 4.1 and 0.4 g/cm^3 for Au and water, respectively. Results of MD simulations relating to calculations of diffusion coefficient D in the overcritical states of gold and gold–water mixture are presented in table 1. Corresponding MD simulations were done using new EAM potential. Positions of corresponding points (where coefficient D was calculated) are marked as magenta rhombus in figure 17.

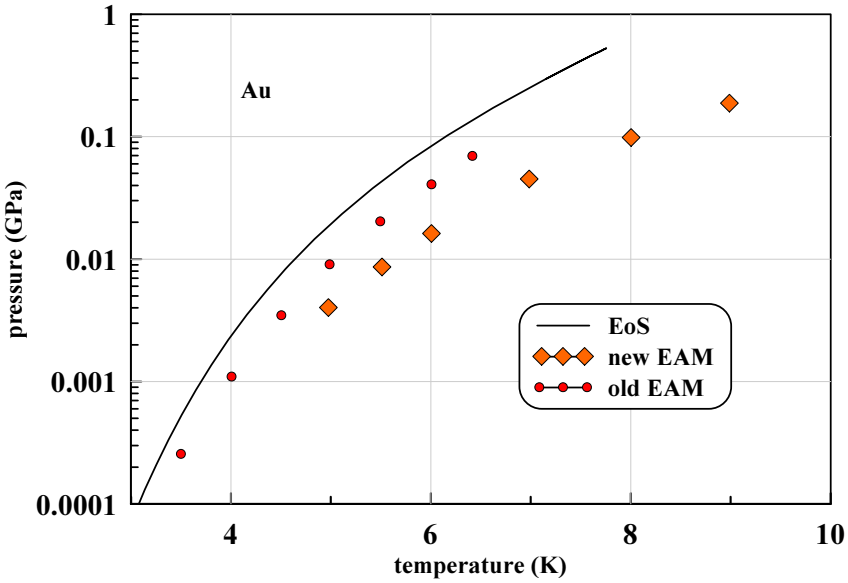

Figure 16. Saturation pressure $p_{\rm sat}(T)$ curves for gold from the wide-range equation of state (EoS) [16–26] and from EAM-MD simulations. The right end points of the curves correspond to the critical points. It is difficult to define $p_{\rm sat}$ from EAM-MD at small pressures much smaller than 1 GPa. Simulation errors in the EAM-MD approach also increase near the critical point.

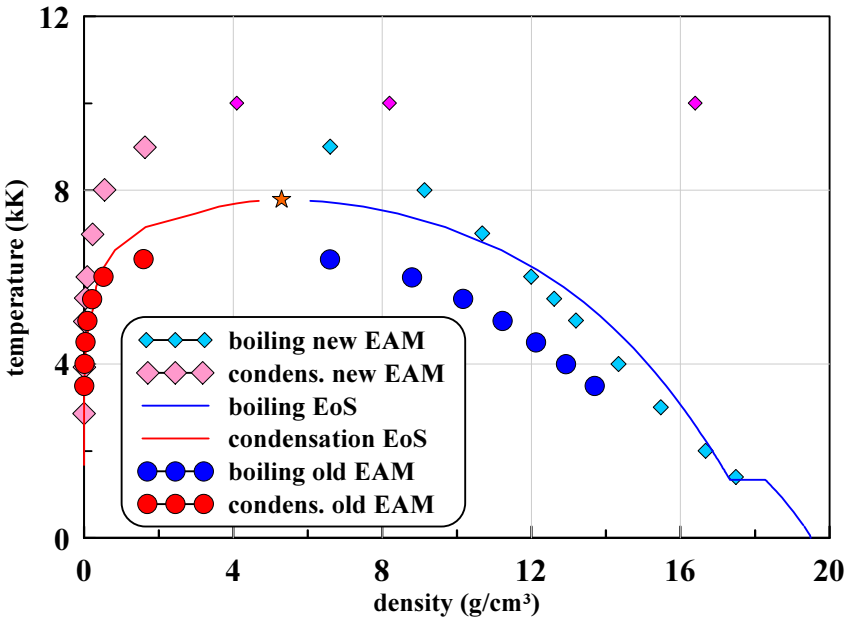

Figure 17. The ρ–T plane of the phase diagram of gold. Comparison of the binodal curves from EAM-MD and EoS. The 3 magenta rhombus shows places where diffusion coefficient in pure Au and Au–wt mixture was evaluated, table 1. EAM-MD reproduces accurately melting temperature of Au.

6. Cooling, condensation, and formation of nanoparticles

There is significant gold–water atomic inter-diffusion mixing process when matter near the CB exist in the overcritical states; see figures 12–15 about duration of residence in the overcritical

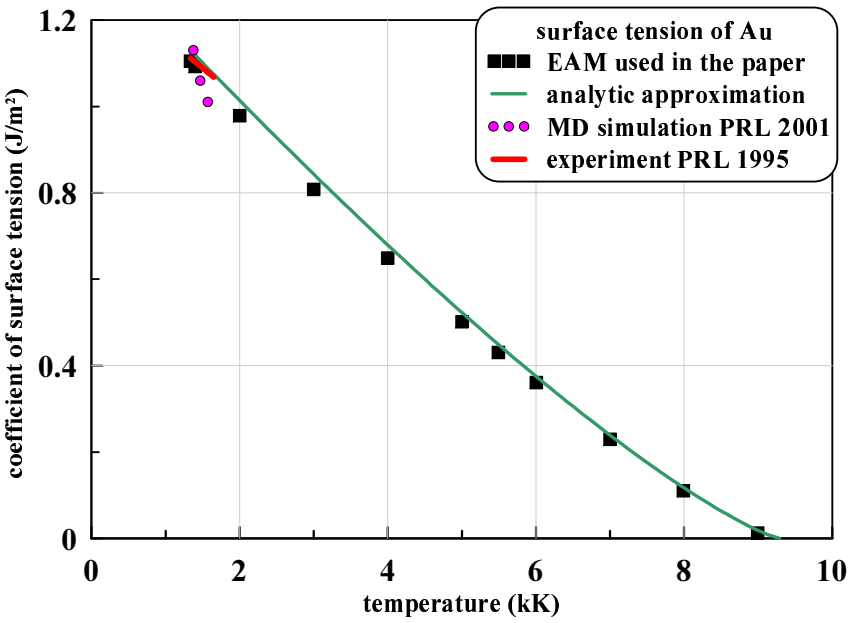

Figure 18. Behavior of surface tension of gold $\sigma(T)$ along the boiling curve shown in figures 16 and 17. Black squares relate to the EAM-MD calculations done using the new EAM potential. Calculation of $\sigma(T)$ by the old EAM is presented in figure 15 in paper [35]. The old EAM gives approximately twice lower values of $\sigma(T)$. See discussion in [42] about evaporation and surface tension. Green continues curve gives approximation $\sigma = \sigma(T_3)((1 - T/T_{\rm cr})/(1 - T_3/T_{\rm cr}))^{5/4}$ from [43], see also [35]. Here T_3 and $T_{\rm cr}$ are temperatures in the triple and critical points. The PRL1995 and 2001 relates to the data from [44,45]. They cover only short temperature intervals.

states and figure 17 with table 1 about the enhanced value of diffusion coefficient D in these states. Thus, the jump like CB diffuses into a smearing layer. The thickness of this layer is $l_{\rm diff} \sim 2\sqrt{D\,t}$. Taking durations t from few to few tens of nanoseconds we obtain values of $l_{\rm diff}$ from few tens to $\sim 10^2$ nm.

Hydrodynamic expansion causes cooling of mixture thanks to work done for expansion. Gradually temperature drops below the critical value for gold. Then condensation into clusters of Au atoms begins. These clusters are in Brownian movement, sometimes meet each other and stick together. Atoms surrounding a cluster condensate to a cluster and evaporate from it, thus mass and energy exchange between atoms and a cluster takes place. Our MD simulations presented below show that temperatures of atoms and clusters are approximately the same. Thus collisional removal of the positive energy excess from growing in size (and hence heating) cluster is fast enough to support equality of temperatures.

The hydrodynamic expansion rate is defined by the gradient of velocity $\mathrm{d}v/\mathrm{d}x$ near the CB. At the nanosecond time scale this gradient is of the order of $\mathrm{d}v/\mathrm{d}x|_{\rm CB} \sim 10^8$ 1/s, see figures 2, 4, and 6. Therefore expansion velocity of the CB diffuse layer $\mathrm{d}v/\mathrm{d}x|_{\rm CB}\, l_{\rm diff}$ is a few meters per second.

Following these conditions, we run several MD simulations to estimate the time interval of nucleation and growth of NPs as pure gold or the 50 : 50 mixture (in concentrations of Au and water) intersect a condensation curve shown in figure 17. Calculations are done using the old EAM potential. Condensation starts with some delay in time after the intersection. Of course, this delay depends on the rate of expansion—in the case of very slow expansion the condensation begins very close to the intersection point.

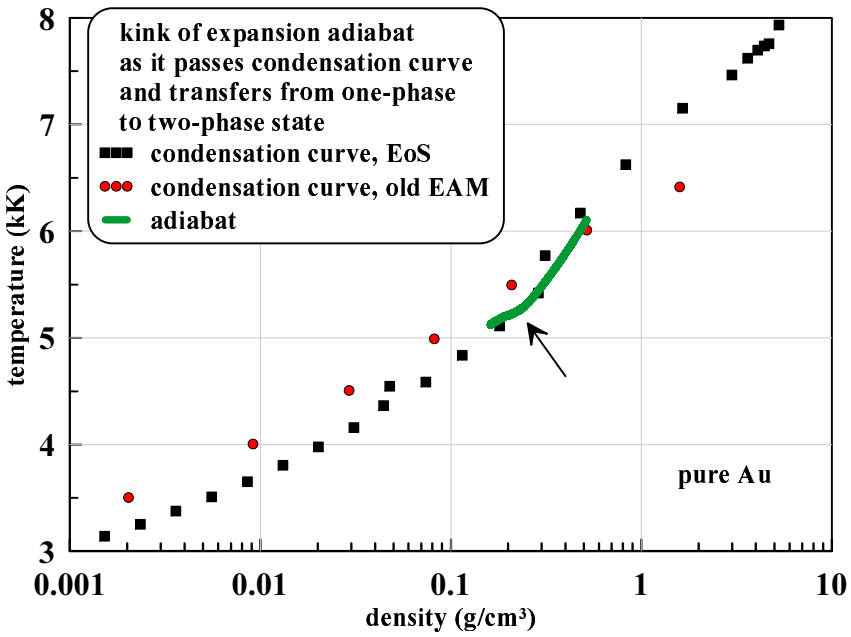

Figure 19. A wide range of the phase diagram showing a small piece of the adiabatic curve near the point where the curve passes through the binodal. The EoS and the old EAM binodals are shown. They are close to each other, near the corresponding intersection point. This EAM-MD simulation is done using the old EAM potential.

Table 2. The list of the points at the adiabatic curve for pure Au in figure 19 and 20. In figure 20, the last three of these points (the three bottom lines here) are marked by the empty squares. These three points correspond to the digits 20.7, 27.3, and 44.2 ns at the maps of potential energy shown in figure 21.

Instant [ns]	T [kK]	p [bar]	ρ [g/cm^3]
0	6.11	436	0.518
20.7	5.32	194	0.254
27.3	5.24	164	0.219
44.2	5.13	126	0.162

Figures 19 and 20 show how the adiabatic curves kink as they pass into the two-phase region. The kink corresponds to the transition from the fast temperature drop with expansion to the slow temperature drop. The fast drop (rather large effective adiabatic index γ) relates to the one-phase behavior (Au is in a gas state). The slow drop (decrease of γ) begins when liquid component appears in a two-phase vapor–liquid mixture. Release of evaporation energy through condensation during volume expansion reduces the rate of temperature decrease.

Figure 19 presents global view of the EoS and old EAM boiling curves and the MD simulated adiabatic curve crossing the boiling curve. The MD simulation is intended for definition of the transition piece from the one-phase to the two-phase behavior along the adiabatic expansion process for our particular conditions: velocity gradient $\sim 10^8$ 1/s and the diffusion thickness of the order of few tens of nm. We are interested to know how long this transition lasts and how large nanoparticles are at the end of our temporal range. The MD simulation is rather difficult

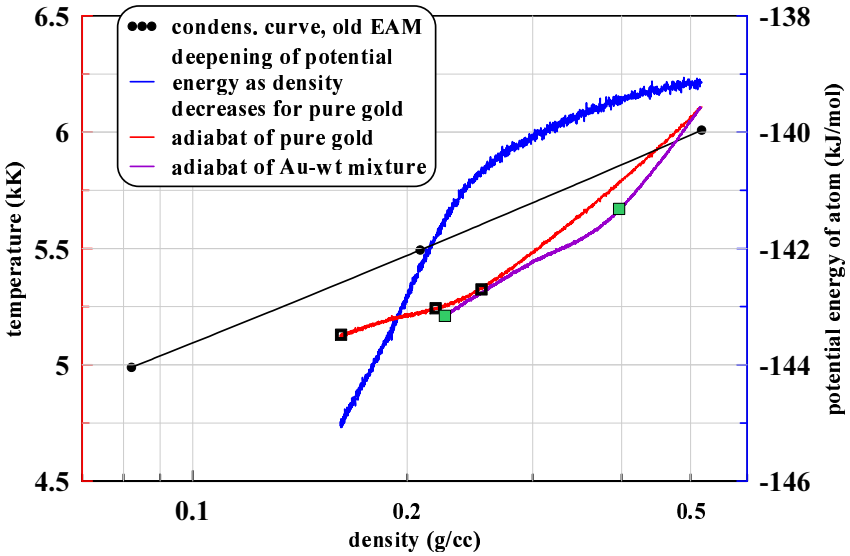

Figure 20. A detailed view of the area near the intersection point taken from figure 19. Two adiabatic curves are presented. One corresponds to pure Au, and the other—to a mixture of 50 : 50 Au and water (in numbers of atoms per unit of volume). The axis of density gives a sum of Au and water densities in the case of a mixture. The condensation curve relates to the case of pure Au, see also figures 17 and 19. It is difficult to find position of the gold condensation curve in case of mixture. It should differ from the binodal for pure gold. Approximately the condensation curve for the 50 : 50 mixture is located slightly above the point where the 50 : 50 adiabatic curve has the kink. Snapshots of the process is demonstrated in figures 21 and 22.

Table 3. The list of the points at the adiabatic curve for Au–water mixture in figure 20. The last two of these points (the two bottom lines) are marked by the filled green squares. These points correspond to the digits 6 and 25.7 ns at the maps of potential energy shown in figure 22. Here the last two columns give total pressure and total density of a mixture (a sum of Au and water contributions).

Instant [ns]	T [kK]	p [bar]	ρ [g/cm^3]
0	6.10	936	0.516
6	5.67	643	0.397
25.7	5.21	324	0.226

because duration is long (tens of ns) and system should consists from large number of atoms $\sim 10^6$. Therefore we limit our self to a narrow time interval just before the intersection (omitting trivial one-phase piece of the gaseous adiabatic curve) and we follow the process during a time scale typical for our problem. This explains why the piece of the adiabatic curve is short in figure 19 relative to the field shown.

Figure 20 demonstrates shape of the two transient kinks at the two adiabatic curves: one for pure Au and another for a mixture Au–wt. The small pieces of the adiabatic curves shown in figure 20 belong to the local vicinities of the points where these two adiabatic curves for pure and mixed Au cross the curves of thermodynamic equilibrium for pure and mixed Au, compare with figure 19. MD simulations with old EAM interatomic potential were used to obtain these two adiabatic curves. The simulation boxes for the both cases have fixed in time periodic boundary

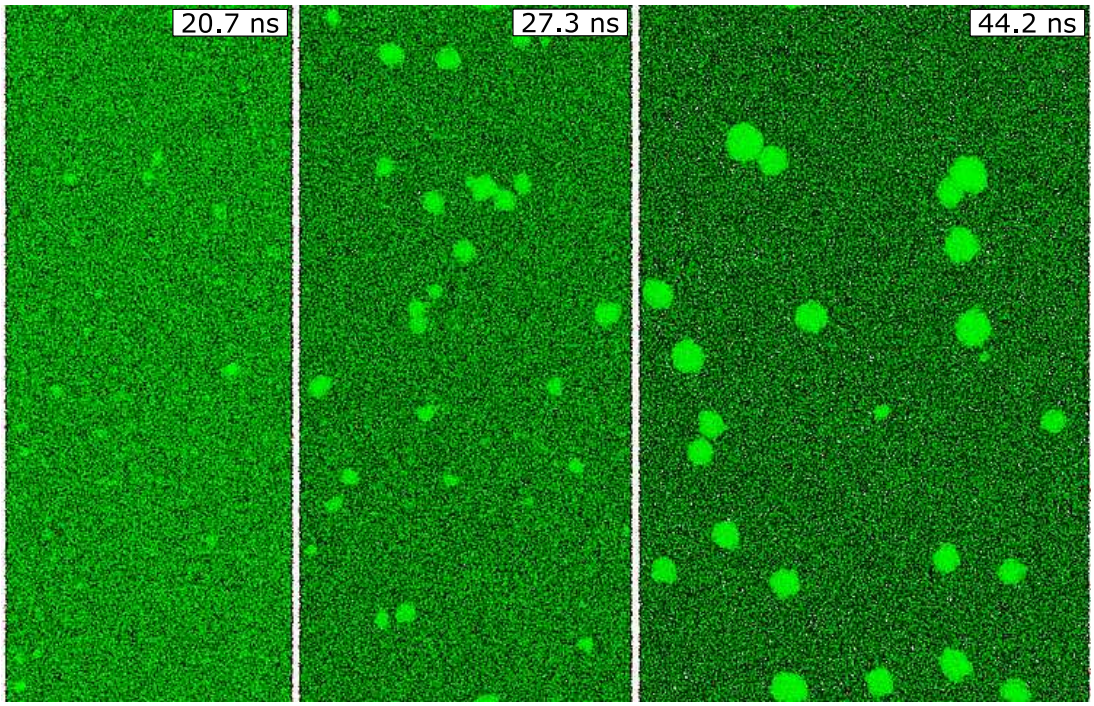

Figure 21. The course of the condensation process with the expansion of the initially gaseous gold. Appearance of the viable clusters begins not immediately as a system of Au atoms crosses an equilibrium curve, see figure 20. Let us mention that unstable (appearing or disappearing) clusters may exist even in gaseous state. They contribute to decrease of pressure relative to pressure of ideal gas with same temperature and atom number density. The three frames shown correspond to the instants listed in table 2 and marked by empty squares in figure 20. The x, y plane is demonstrated. Horizontal direction of expansion is x. Its expansion velocity is 2 m/s. Vertical size along y-axis is 200 nm.

conditions at the lateral walls, i.e., in the y and z directions. Lateral y and z dimensions are 200 and 100 nm, respectively. The moving walls are imposed in the x direction. There are reflecting potentials connected with these x-walls. They return the Au or Au and water atoms colliding the x-wall back into a box. Reflection from the expanding walls extracts small (velocity of expansion is much less than thermal velocity) part of kinetic energy of colliding atoms thus adiabatically cooling a whole system in the box.

The initial densities and temperatures are shown in figure 20 and listed in tables 2 and 3. The initial distance between the x-walls is $\Delta x_0 = 40$ nm. This starting distance is the same in pure Au and the mixture cases. Expansion velocity $v_x|_{\text{expan}} = \mathrm{d}\Delta x/\mathrm{d}t$ is 2 m/s. It is also the same in the both case. Distance between the x-walls grows with time and density decreases $\rho = \rho_0 \Delta x_0/(\Delta x_0 + v_x|_{\text{expan}}\, t)$. This is a model of spatial expansion of pure gold or diffusion mixture in real conditions during expansion and cooling.

Figures 21 and 22 present pictures of evolutions in the direction of condensation of pure Au and mixed systems, respectively. Figures 21 and 22 show how nanoparticles nucleate and grow. The figures correspond to the view along the z-axis. The simulation box is 100 nm long in the z-direction. Figures 21 and 22 are composed from the x, y set of the individual pixels. Every pixel contains information about potential energy averaged along the z-direction. Lighter green pixel marks position where potential energy is deeper. The light green spots are the nanoparticles (NP); indeed, the stuck together atoms of gold have lower potential energy than individual

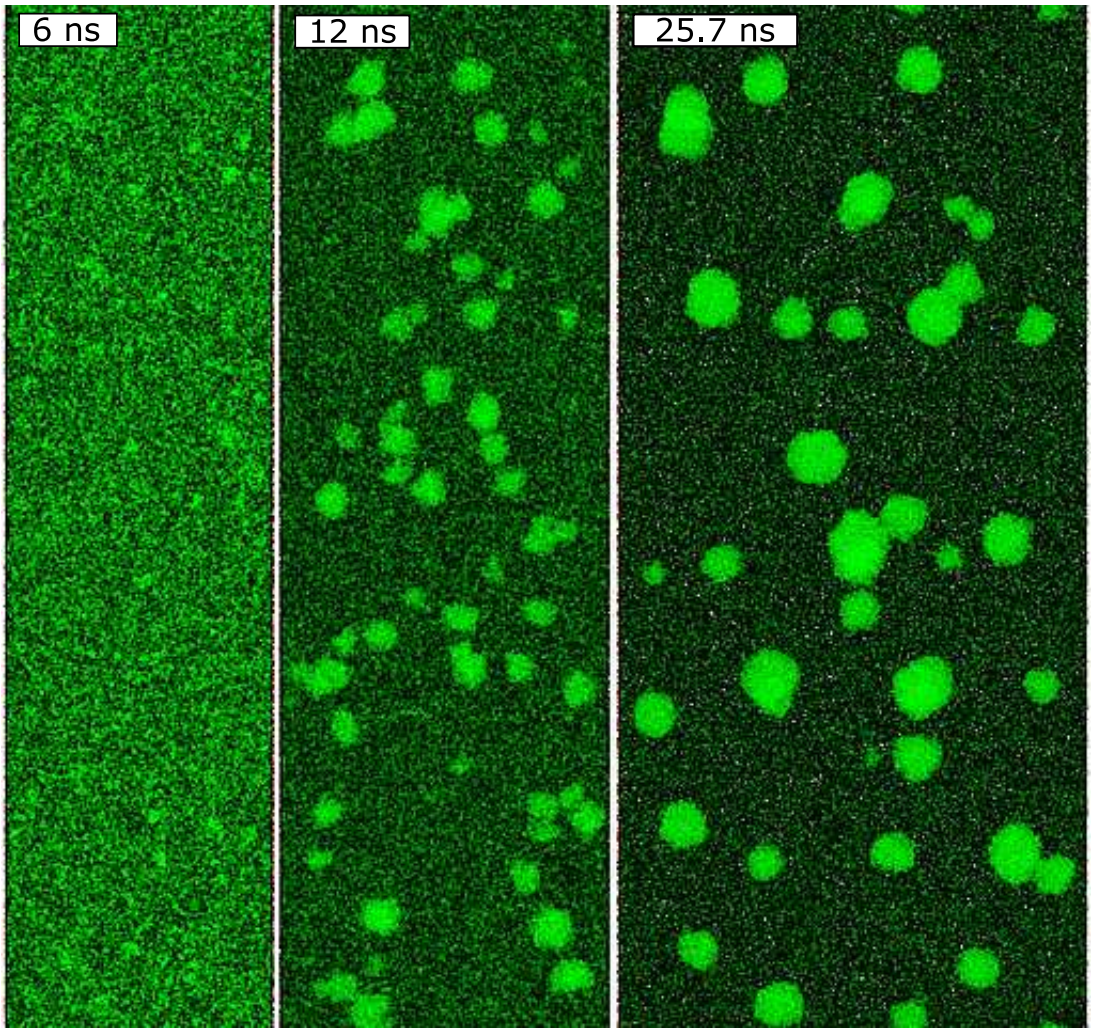

Figure 22. Condensation into gold nanoparticles as Au–water mixture at the ρ–T phase plane decreases below the equilibrium curve for gold in mixture. The left and right frames relate to the two green squares in figure 20, see also table 3. We add the intermediate frame $t = 12$ ns to better show the process of nanoparticles (NPs) formation and growth. Sizes of NPs may be estimated by direct measuring, compare with the vertical dimension (this is the y axis) of the computational box equal to 200 nm. Adiabatic expansion proceeds along the horizontal direction (this is the x axis) expanding with velocity 2 m/s.

atoms. Their sizes are of the order of ten nanometers at the final stages in both cases of pure Au (see figure 21) or Au–water mixture (see figure 22). Atoms sticking together into NP have profit in their interaction energy. Sticking of part of Au atoms in the two-phase system does deeper potential energy of the whole system (averaging along x, y, z-directions). This is shown in figure 20 by the dependence relating to potential energy. Figures 21 and 22 show the same but with averaging only along the z-direction. Temperatures in figures 21 and 22 are higher than melting temperature of gold. Therefore, NP remains in liquid state in the temporal range considered.

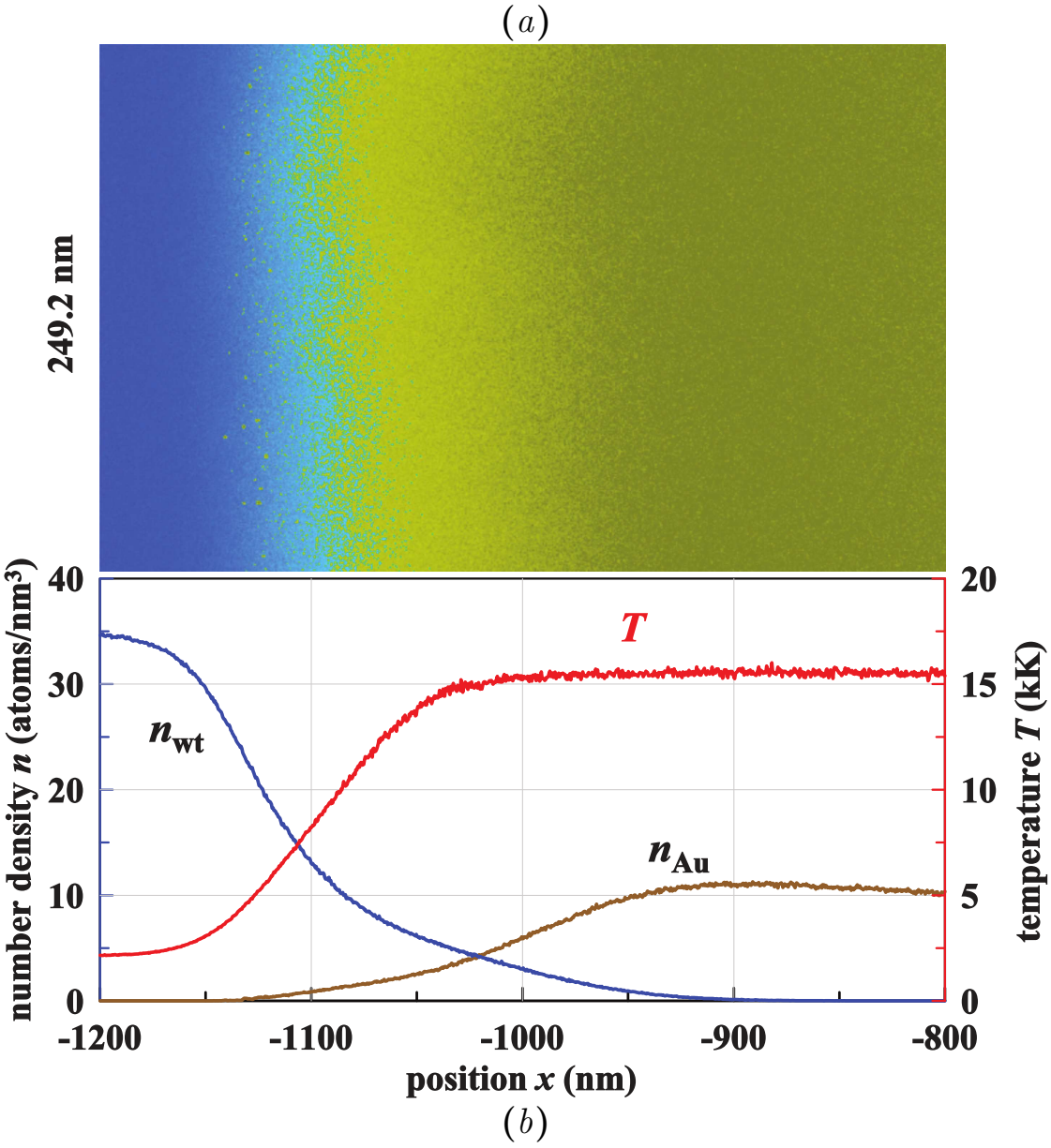

Figure 23. The top panel (a) illustrates a snapshot at $t = 950$ ps of the atomic number density map of Au (yellow color) moving to the left with velocity ≈ 700 m/s at that instant; degrees of yellow are proportional to local atomic density presented in the bottom panel (b). Au displaces water which resists to displacement and thus causes deceleration of Au. Deceleration and density difference are the reasons that result in appearance of Rayleigh–Taylor instability (RTI) evidently seen [8, 9, 11] at the lower values of $F_{\rm abs}$. Surface tension imposes clear capillary spatial scale for the growing perturbations [8, 9, 11]. But here at enhanced laser action the diffusion is stronger and it suppresses development of RTI while the capillary scale shrinks to zero. The bottom panel gives the number densities instant profiles of Au and water atoms corresponding to the instant shown in the upper panel. The map from the upper panel is integrated in the lateral dimensions for Au and water separately to obtain these profiles.

7. Molecular dynamics simulation of ablation in water

From the sequence of three shots compared in figures 9, 10 and 12–15 we see that increase of absorbed energy $F_{\rm abs}$ causes serious consequences. The main feature is that with this increase a metal near a CB transfers from undercritical to overcritical conditions and remains their for rather long time. Undercritical (condensed) and overcritical (uncondensed, gaseous) conditions differ qualitatively. In the undercritical case (relatively small $F_{\rm abs}$) the liquid gold contacts with liquid; our fluences are above melting threshold for Au. Thus to penetrate into liquid and to form NPs the Au atoms have to overcome surface barrier through evaporation or dissolution (the first step) and after that they diffusively drift out from a CB (the second step). At the last step the expansion and cooling lead to condensation and formation of NPs, figures 20 (adiabatic curve in case of mixture, intersection of the condensation curve) and 22 (condensation in case of mixture).

In overcritical states, the first step disappears along with surface tension. It is very important. Indeed, low values of saturated pressures of evaporated or dissolved Au atoms outside the boundary of a continuous condensed phase (outside the CB) strongly limits amount of Au atoms in a diffusion layer and thus limits amount of NPs. In the overcritical states only the second and third steps are present. This enhances diffusion—now diffusion starts not from evaporated or dissolved atomic number density of Au near the CB but from much larger value of atomic number density directly in the continuous phase (atomically sharp boundary disappears together with surface tension, see figure 18).

We perform a large scale MD simulation to follow the ablation of gold into water at absorbed energy $F_{\rm abs}$ larger than in the case previously considered in paper [11]. Here in figure 23 rather late instant from MD simulation with large $F_{\rm abs}$ is presented. We see that Au–water interpenetration significantly overcomes the estimate $l_{\rm diff} = 2\sqrt{D\,t} = 20$ nm for $D = 10^{-3}$ cm^2/s and $t = 1$ ns. May be enhancement of interpenetration is due to presence of some embryos of Rayleigh–Taylor instability. Indeed, it is known that diffusion is a laminar like process which produces very flat atomically mixed layer; diffusion smoothes away lateral roughness. But in figure 23, we see significant inhomogeneities in the direction transverse to the direction of longitudinal expansion.

8. Conclusions

The laser ablation of Au into transparent media is analyzed. Initial stages of the NP formation are considered. These stages relate to tens and hundreds of nanoseconds well before the bubble dynamics come into play. All thermodynamic (with first order phase transitions) and hydrodynamic aspects have to be included to come to understanding of appearance of primary NPs. It is found following:

- Deceleration of the CB at the nanosecond time scale is approximately exponential $v_{\rm CB} \propto \exp(-t/t_{\rm dec})$ with the e-folding time $t_{\rm dec}$ of the order of 0.5–1 ns. This law describes deceleration in the 1–0.1 km/s range of velocities $v_{\rm CB}$ after ultrashort and subnanosecond pulses.
- Maximum shift of the CB from its initial position is rather limited and it is of the order of micron.
- Temperature $T_{\rm CB}$ of gold at the CB nonlinearly depends on absorbed energy $F_{\rm abs}$; $T_{\rm CB}$ strongly increases for energies $F_{\rm abs} \sim 1$ J/cm^2 up to values $\sim 10^5$ K for subnanosecond laser pulses. These values are much above critical temperature. While the density of gold $\rho_{\rm CB}$ decreases down to values ~ 1 g/cm^3.
- Ablation motion triggered by a subnanosecond pulse is order of magnitude more stable against Rayleigh–Taylor instability (RTI) in comparison with an ultrashort action. This

is simply caused by the shortening of deceleration stage because more than a half of the heating pulse is spent to accelerate the CB.

- Another important reason to limit the RTI perturbations growth is connected with high temperatures, decrease of the density ratio at the CB, and enhancement of diffusion. Enhanced diffusion is a powerful stabilizer of RTI. Diffusive smearing grows as $l \propto t^{1/2}$ while for RTI in the case with permanent deceleration the law of growth is $l \propto t^2$. Thus diffusion always dominates at the early stages while the RTI wins this competition later in time. But in laser ablation the deceleration quickly decays in time. Thus there is only limited interval of times when perturbations can develop thanks to RTI. In this situation the diffusion process suppresses RTI. Then RTI is removed from the process of fabrication of NPs at the capillary scale. The appearance of NPs of the capillary scale was observed in simulations [8–11].

References

[1] Stuart B C, Feit M D, Rubenchik A M, Shore B W and Perry M D 1995 *Phys. Rev. Lett.* **74** 2248–51
[2] Smith A V and Do B T 2008 *Appl. Opt.* **47** 4812–32
[3] Zhang D, Gökce B and Barcikowski S 2017 *Chem. Rev.* **117** 3990–4103
[4] Xiao J, Liu P, Wang C X and Yang G W 2017 *Prog. Mater. Sci.* **87** 140–220
[5] Lam J, Lombard J, Dujardin C, Ledoux G, Merabia S and Amans D 2016 *Appl. Phys. Lett.* **108** 07410
[6] Povarnitsyn M E, Itina T E, Levashov P R and Khishchenko K V 2013 *Phys. Chem. Chem. Phys.* **15** 3108–14
[7] Povarnitsyn M E and Itina T 2014 *Appl. Phys.* A **117** 175–8
[8] Shih C Y, Shugaev M V, Wu C and Zhigilei L V 2017 *J. Phys. Chem.* C **121** 16549–67
[9] Shih C Y, Streubel R, Heberle J, Letzel A, Shugaev M V, Wu C, Schmidt M, Gokce B, Barcikowski S and Zhigilei L V 2018 *Nanoscale* **10** 6900–10
[10] Inogamov N, Zhakhovsky V and Khokhlov V 2018 Laser ablation of gold into water: near critical point phenomena and hydrodynamic instability arXiv:1803.07343v1 [physics.comp-ph]
[11] Inogamov N A, Zhakhovskii V V and Khokhlov V A 2018 *J. Exp. Theor. Phys.* **127** 79–106
[12] Inogamov N A, Zhakhovsky V V, Ashitkov S I, Khokhlov V A, Shepelev V V, Komarov P S, Ovchinnikov A V, Sitnikov D S, Petrov Yu V, Agranat M B, Anisimov S I and Fortov V E 2011 *Contrib. Plasma Phys.* **51** 367–74
[13] Demaske B J, Zhakhovsky V V, Inogamov N A and Oleynik I I 2013 *Phys. Rev.* B **87** 054109
[14] Karim E T, Shugaev M, Wu C, Lin Z, Hainsey R F and Zhigilei L V 2014 *J. Appl. Phys.* **115** 183501
[15] Karim E T, Shugaev M V, Wu C, Lin Z, Matsumoto H, Conneran M, Kleinert J, Hainsey R F and Zhigilei L V 2016 *Appl. Phys.* A **122** 407
[16] Bushman A V, Fortov V E, Kanel G I and Ni A L 1993 *Intense Dynamic Loading of Condensed Matter* (London: Taylor & Francis)
[17] Khishchenko K V 1997 *High Temp.* **35** 991–4
[18] Khishchenko K V, Tkachenko S I, Levashov P R, Lomonosov I V and Vorob'ev V S 2002 *Int. J. Thermophys.* **23** 1359–67
[19] Khishchenko K V 2004 *Tech. Phys. Lett.* **30** 829–31
[20] Levashov P R, Khishchenko K V, Lomonosov I V and Fortov V E 2004 *AIP Conf. Proc.* **706** 87–90
[21] Levashov P R, Khishchenko K V and Lomonosov I V 2006 *AIP Conf. Proc.* **849** 353–7
[22] Levashov P R and Khishchenko K V 2007 *AIP Conf. Proc.* **955** 59–62
[23] Khishchenko K V 2008 *J. Phys.: Conf. Ser.* **98** 032023
[24] Khishchenko K V 2015 *J. Phys.: Conf. Ser.* **653** 012081
[25] Lomonosov I V and Fortova S V 2017 *High Temp.* **55** 585–610
[26] Khishchenko K V 2017 *Math. Montis.* **40** 140–7
[27] URL `www.researchgate.net/project/Development-of-interatomic-EAM-potentials`
[28] Yasuoka K and Matsumoto M 1998 *J. Chem. Phys.* **109** 8451
[29] Anisimov S I and Luk'yanchuk B S 2002 *Phys. Usp.* **45** 293–324
[30] Lummen N and Kraska T 2004 *Nanotechnology* **15** 525
[31] Zhakhovsky V V, Kryukov A P, Levashov V Yu, Shishkova I N and Anisimov S I 2018 *Proc. Natl. Acad. Sci. U. S. A.* **116** 18209–17
[32] Povarnitsyn M E, Fokin V B and Levashov P R 2015 *Appl. Surf. Sci.* **357** 1150–6
[33] Povarnitsyn M, Fokin V, Levashov P and Itina T 2015 *Phys. Rev.* B **92** 174104

[34] Khokhlov V A, Inogamov N A, Zhakhovsky V V, Shepelev V V and Ilnitsky D K 2015 *J. Phys.: Conf. Ser.* **653** 012003
[35] Inogamov N A, Zhakhovskii V V and Khokhlov V A 2015 *J. Exp. Theor. Phys.* **120** 15–48
[36] Wang X W, Kuchmizhak A A, Li X, Juodkazis S, Vitrik O B, Kulchin Yu N, Zhakhovsky V V, Danilov P A, Ionin A A, Kudryashov S I, Rudenko A A and Inogamov N A 2017 *Phys. Rev. Appl.* **8** 044016
[37] Li Q, Alloncle A P, Grojo D and Delaporte P 2017 *Opt. Express* **25** 24164–72
[38] Li Q, Alloncle A P, Grojo D and Delaporte P 2017 *Appl. Phys.* A **123** 718
[39] Rouleau C M, Shih C Y, Wu C, Zhigilei L V, Puretzky A A and Geohegan D B 2014 *Appl. Phys. Lett.* **104**
[40] Schrider K J, Torralva B and Yalisove S M 2015 *Appl. Phys. Lett.* **107** 124101
[41] Petrov Yu V, Inogamov N A and Migdal K P 2013 *JETP Lett.* **97** 20–7
[42] Anisimov S I, Dunikov D O, Zhakhovskii V V and Malyshenko S P 1999 *J. Chem. Phys.* **110** 8722–9
[43] Semenchenko V K 1961 *Surface Phenomena in Metals and Alloys* (New York: Pergamon)
[44] Egry I, Lohoefer G and Jacobs G 1995 *Phys. Rev. Lett.* **75** 4043–6
[45] Webb III E B and Grest G S 2001 *Phys. Rev. Lett.* **86** 2066–9
[46] Zhakhovskii V V, Inogamov N A, Petrov Yu V, Ashitkov S I and Nishihara K 2009 *Appl. Surf. Sci.* **255** 9592–6